Ultrasound Imaging of Cardiac Fiber Orientation: What are We Looking at?

Ultrasound imaging of cardiac fiber orientation: What are we looking at?

Alessandro Ramalli
Lab. on Cardiovascular Imaging & Dynamics, Dept. of Cardiovascular Sciences, KU Leuven
Leuven, Belgium
alessandro.ramalli@kuleuven.be

Pedro Santos
Lab. on Cardiovascular Imaging & Dynamics, Dept. of Cardiovascular Sciences, KU Leuven
Leuven, Belgium

Jan D'hooge
Lab. on Cardiovascular Imaging & Dynamics, Dept. of Cardiovascular Sciences, KU Leuven
Leuven, Belgium

***Abstract*— Myocardial tissue is very complex: sarcomeres are linked to form myofibrils that combine into myocytes that, in turn, group into muscle fibers; the latter are organized in a complex 3D network governing cardiac mechanics and thereby function. As such, cardiac fiber imaging might be an important diagnostic tool. Hereto, Papadacci et al. enabled the assessment of the transmural fiber orientation during the cardiac cycle by 3D Backscatter Tensor Imaging; however, which histologic structure it detects remains unclear. The aim of this work was therefore to propose and validate, by computer simulation, a theoretical framework that addresses this issue. Field II simulations were carried out by modeling a 32×32 array while numeric phantoms were developed to mimic cardiac fibers and their orientation. Examples of spatial coherence (SC) maps are presented clearly showing their dependency on fiber pitch (P) and size (S). Indeed, the main-to-secondary lobe distance of the SC function linearly correlates with P (R^2=99%) while the width of the main lobe linearly correlates with S (R^2=92%). Transmural fiber orientation was also assessed with an overall RMSE and absolute error lower than 3.3° and 1.1° respectively. In conclusion, as predicted by the proposed theory, the SC maps not only allow assessing the local fiber direction but also allow estimating fiber pitch and size thus providing information on the microstructures being investigated.**

Keywords*— *Fiber orientation, Cardiac imaging, Plane waves, Spatial coherence.

I. Introduction

Cardiovascular diseases remain the leading cause of death in the world and thus have a tremendous impact on our society [1], [2]. Major diseases are often associated with a reduced ability of the left ventricle to pump blood to the body, due to a reduced contractility of the myocardium. Its tissue is very complex: sarcomeres are linked to form myofibrils that combine into (cardio-) myocytes that, in turn, group into muscle fibers; the latter are organized in a complex 3D network [3]. Although the exact organization of cardiac fibers in a 3D network (myoarchitecture) has been much debated [4]–[6], cardiologists have been aware, for at least a century, of the evidence that fiber orientation varies across the myocardial walls [7], [8]. Such a complex organization of cells is linked to the mechanical and electrical properties of the heart, determining its function [9]–[11]; moreover, an abnormal fiber orientation or disarray is found in different pathologies [12]–[14]. Thus, the study of fiber orientation is of primary interest for the understanding of cardiac pathophysiology and for the early diagnosis of cardiac diseases.

Almost all the medical imaging methodologies have developed a specific technique for the estimation of cardiac fiber orientation: magnetic resonance imaging [15], [16], x-ray [17], [18], optical tomography [19], [20], microscopy [21], [22], and ultrasound [23]–[25]. However, all of them present at least one major limit, such as invasiveness, limited size of the region of interest, low resolution, low frame rate, that still hamper their implementation in clinical routine.

In ultrasound imaging, the state-of-the-art can be considered [25]; here Papadacci et al. showed promising results of the orientation of the cardiac fiber during the cardiac cycle. They overlaid cardiac fiber orientation values to standard M-mode and showed in-vivo results on an open chest sheep, showing how the fiber orientation changes during the cardiac cycle, due to an increase in the wall thickness. In addition, they also succeeded in mapping the myocardial fiber orientation in 3D of the in-vivo human heart both in systole and in diastole during transthoracic imaging. Their proposed method, called 3D ultrasound Backscatter Tensor Imaging (3D-BTI), is based on ultrafast volumetric acquisitions, which are exploited to quantify the spatial coherence of backscattered echoes at each point of the volume. The theoretical base of 3D-BTI was previously reported in [26], [27] and relies on the estimation of the spatial coherence of echo signals received from a focused transducer.

Nevertheless, which histologic structure 3D-BTI detects remains unclear. Therefore, the aim of our work was to propose and validate, by computer simulation, a theoretical framework to address this issue.

The paper is organized as follows: section II introduces the theoretical background, the simulation settings, and the post-processing algorithms; section III shows simulation results; section IV presents discussion and conclusions.

II. Methods

A. Theoretical background

In the next paragraphs, we relate the autocorrelation of the backscattered signals to the spatial coherence (SC) of a tissue under exam when transmitting a plane wave. We will follow a procedure similar to that described in [27]–[29] that derived such relation for a focused transducer; the procedure will be split in three steps: 1) transmission; 2) reflection & backpropagation; 3) autocorrelation & spatial coherence.

This work was supported by the European Union's Horizon 2020 research and innovation programme under the Marie Skłodowska-Curie grant agreement No 786027 (ACOUSTIC project) and by Internal Funds University of Leuven grant (PF/10/014).

DOI: 10.1109/ULTSYM.2018.8580100

1) Transmission

Durnin [30] demonstrated that, in a Cartesian coordinate system (*x,y,z*),

$$E(x,y,z,t) = J_0\left(\alpha \cdot \sqrt{x^2+y^2}\right) \cdot e^{j(\beta z - \omega t)} \quad (1)$$

is an exact solution of the wave equation for free space

$$\left(\nabla^2 - \frac{1}{c^2}\frac{\partial^2}{\partial t^2}\right) E(x,y,z,t) = 0 \quad (2)$$

Where c is the speed of sound, ω is the angular frequency, β is the propagation constant, $J_0(\cdot)$ is the zero-order Bessel function of the first kind and α is a scaling parameter that determines the width of the main lobe of the Bessel function, subjected to $\beta^2 + \alpha^2 = \omega^2/c^2$. Equation (1) represents a class of nondiffracting beams (or limited diffraction beams [31]) in the sense that the intensity profile at $z = 0$ is exactly reproduced for all $z > 0$, i.e. in every plane normal to the z axis. Nevertheless, these solutions represent waves propagating to an infinite distance without diffraction, provided that they are produced with an infinite aperture and with infinite energy [31]. However, even when limited diffraction beams are produced with a finite aperture, they have a large depth of field (z_{DOF}) and an approximate depth-independent lateral profile, i.e., they have approximately unchanged beam shapes over a large axial distance [32].

In particular, when $\alpha = 0$, (1) reduces to the equation of a plane wave:

$$E(z \geq 0, t) = e^{j(\beta z - \omega t)} \quad (3)$$

Therefore, the plane wave transmitted by a square aperture results:

$$E(x,y,z \geq 0, t) = \Pi\left(\frac{x}{A}\right) \cdot \Pi\left(\frac{y}{A}\right) \cdot e^{j(\beta z - \omega t)} \quad (4)$$

Where A is the side of the aperture and $\Pi(x)$ is the rectangular function defined as:

$$\Pi(x) = \begin{cases} 1, & if\ |x| < 1/2 \\ 0, & if\ |x| \geq 1/2 \end{cases} \quad (5)$$

From (4), neglecting the wave propagation term and defining z_F as the depth of the plane where the fibers are located, the module of the incidence acoustic field for any $z_F \leq z_{DOF}$ can be approximated as:

$$E_I(x,y,z_F \leq z_{DOF}) = \Pi\left(\frac{x}{A}\right) \cdot \Pi\left(\frac{y}{A}\right) \quad (6)$$

2) Reflection & backpropagation

In the random mirror approach [27, Sec. I], defining $\eta(x,y)$ a random variable representing the backscattering amplitude of the fiber plane [33], the reflected field module at the fiber plane depth is:

$$E_R(x,y,z_F) = E_I(x,y,z_F) \cdot \eta(x,y) \quad (7)$$

Then, within the Fresnel's approximation [27], [34], [35, Ch. 4], [36, Ch. 6], the propagation of a wave field, from two parallel planes divided by a distance z, can be approximated by a spatial impulse response:

$$h_z(x,y,z) = \frac{e^{jkz}}{j\lambda z} \cdot e^{j\frac{\pi}{\lambda z}(x^2+y^2)} \quad (8)$$

Hence, the backpropagated field on the plane of the receiving probe is:

$$E_B(x,y,0) = E_R(x,y,z_F) \otimes h_z(x,y,z_F), \quad (9)$$

the 2D Fourier transform ($\mathcal{F}_{2D}\{\cdot\}$) of which, according to the convolution ($\otimes$) theorem, is:

$$\begin{aligned} &\mathcal{F}_{2D}\{E_B(x,y,0)\} = \\ &= \mathcal{F}_{2D}\{E_R(x,y,z_F)\} \cdot \mathcal{F}_{2D}\{h_z(x,y,z_F)\} \end{aligned} \quad (10)$$

3) Autocorrelation & spatial coherence

Defining the continuous autocorrelation of a function $g(t)$

$$R\{g(t)\} = R_g(t) \stackrel{\text{def}}{=} \int g^*(\tau) \cdot g(t+\tau)\, d\tau, \quad (11)$$

its Fourier transform results

$$\mathcal{F}\{R_g(t)\} = \mathcal{F}\{g(t)\} \cdot \mathcal{F}^*\{g(t)\}. \quad (12)$$

Extending the latter to the autocorrelation of a function $g(x,y)$ defined in the 2D space domain we obtain the following equation:

$$\mathcal{F}_{2D}\{R_g(x,y)\} = \mathcal{F}_{2D}\{g(x,y)\} \cdot \mathcal{F}^*_{2D}\{g(x,y)\}, \quad (13)$$

Then, after a few intermediate steps (refer to Appendix A) we can demonstrate that

$$\begin{aligned} &\mathcal{F}_{2D}\{R_{E_B}(x,y,0)\} = \\ &\mathcal{F}_{2D}\{R_{E_R}(x,y,z_F)\} \cdot \mathcal{F}_{2D}\{R_{h_z}(x,y,z_F)\}. \end{aligned} \quad (14)$$

In other words, the 2D Fourier transform of the autocorrelation of the backpropagated field on the probe plane ($\mathcal{F}_{2D}\{R_{E_B}(x,y,0)\}$) is given by the product of the 2D Fourier transforms of the autocorrelation of the reflected field ($\mathcal{F}_{2D}\{R_{E_R}(x,y,z_F)\}$) and of the propagation spatial impulse ($\mathcal{F}_{2D}\{R_{h_z}(x,y,z_F)\}$). Nevertheless, the latter term can be neglected since

$$\begin{aligned} &\mathcal{F}_{2D}\{R_{h_z}(x,y,z_F)\} = \\ &= \mathcal{F}_{2D}\{h_z(x,y,z_F)\} \cdot \mathcal{F}^*_{2D}\{h_z(x,y,z_F)\} = \\ &= |\mathcal{F}_{2D}\{h_z(x,y,z_F)\}|^2 = \left|e^{jkz} \cdot e^{-j\pi\lambda z(f_x^2+f_y^2)}\right|^2 = \\ &= 1 \end{aligned} \quad (15)$$

where f_x and f_y are the spatial frequencies along x and y directions. Finally, from (14), it follows that

$$\mathcal{F}_{2D}\{R_{E_B}(x,y,0)\} = \mathcal{F}_{2D}\{R_{E_R}(x,y,z_F)\} \quad (16)$$

and hence, from (16), (7) and (6), that

$$\begin{aligned} R_{E_B}(x,y,0) &= R_{E_R}(x,y,z_F) = \\ &= R\{E_I(x,y,z_F) \cdot \eta(x,y)\} = \\ &= R\left\{\Pi\left(\frac{x}{A}\right) \cdot \Pi\left(\frac{y}{A}\right) \cdot \eta(x,y)\right\} \end{aligned} \quad (17)$$

In other words, the autocorrelation of the backpropagated field on the probe plane (also called spatial coherence, SC) is equal to the autocorrelation of the backscattering amplitude of the fiber plane in the region illuminated by the plane wave.

B. Simulations

1) Numeric phantom

In order to validate the proposed theoretical framework, we developed a numeric phantom to simulate cardiac fibers and their orientation through the myocardium. The phantom has a parallelepiped shape and contains two sets of scatterers, respectively defining the background and the fibers. The background consists of randomly placed scatterers with a Gaussian scattering amplitude distribution. The fibers, so as to ensure phase continuity, are modeled by scatterers that are placed on a regular grid, while their scattering amplitude $\eta(x,y)$ is modulated according to a periodic function:

$$\eta(x,y) = III_P(x) \otimes \Pi\left(\frac{x}{S}\right) \tag{18}$$

where $III_P(x)$ is the Dirac comb function of period P (i.e. the fiber pitch) and S is the fiber size. It is worth highlighting that the above scattering map has a fixed orientation, i.e. the fibers are aligned along the direction y; hence, in order to introduce a different orientation angle in layers at different depths, the scattering amplitude map is rotated in the plane x-y by the angle:

$$\varphi(z) = \varphi_0 + \frac{\partial\varphi}{\partial z} \cdot round\left(\frac{z}{S}\right) \cdot S \tag{19}$$

where $\partial\varphi/\partial z$ is the fiber orientation rate with respect to the transmural position and φ_0 is the initial fiber orientation angle. Hence, the fibers are arranged in sheets of fibers as thick as the fiber size.

2) Setup

In this work, Matlab (The MathWorks, Natick, MA, USA) simulations with Field II [33], [37] were carried out by modeling a 32×32-element 2D array with 300 µm pitch; its impulse response was defined as 2.5-cycle Hamming-weighted sinusoidal burst at 3 MHz, corresponding to a relative bandwidth of 73%. A 1-cycle Hamming-weighted sinusoidal burst at 3 MHz was used as the excitation signal. The sampling frequency was set to 30 MHz; a non-steered plane wave was transmitted; and the received echo signals saved for post-processing.

The phantom, centered at a depth of 60 mm, had a size of 10×10×6 mm^3, respectively along x, y, and z. The step of the regular grid was set to 50 µm, i.e. one tenth of the wavelength, corresponding to a density of 8M-scatterers per cm^3. The same density was set for the randomly placed scatterers belonging to the background whose intensity was set 20dB lower than that of the fibers.

Different S values (200, 400, 600 µm) and P values (400, 800, 1200, 1600, 2000 µm) were considered subject to the condition $P>2S$. The orientation of the fiber was set so that $\varphi_0 = 60°$ and $\partial\varphi/\partial z = 10°/\text{mm}$.

C. Post-processing

1) Spatial coherence

The spatial coherence of backscatter signals was computed according to the formulation reported in [25]:

$$R(\Delta x, \Delta y) = \frac{1}{(N_x - |\Delta x|)\cdot(N_y - |\Delta y|)} \cdot \tag{20}$$

$$\cdot \sum_{x_i}\sum_{y_i} \frac{\sum_{t=T_1}^{T_2} S_{RF}(x_i, y_i, t)\cdot S_{RF}(x_i - \Delta x, y_i - \Delta y, t)}{\sqrt{\sum_{t=T_1}^{T_2} S_{RF}(x_i, y_i, t)^2 \cdot S_{RF}(x_i - \Delta x, y_i - \Delta y, t)^2}}$$

Where $S_{RF}(x_i, y_i, t)$ is the radiofrequency echo signal received on the i-th element with coordinates x_i, y_i, while T_1 and T_2 are the two ends of the averaging temporal window. It is worth highlighting that, according to the proposed theory, $S_{RF}(x_i, y_i, t)$ is the signal as it is received, without applying any dynamic focusing delay.

2) Fiber orientation estimation

As suggested in [25], the fiber orientation was estimated as the angle corresponding to the maximum of the Radon transform [38, Ch. 2] of the 2D spatial coherence function. In particular, the processing was completed in several steps, as illustrated in Fig. 1. The processing starts from the spatial coherence map, that is first interpolated (I) and then tapered with a Tukey window with circular symmetry (II). Then it is transformed through a Radon transform (III), computed in the range [-90°,90°]; finally, the estimated fiber orientation corresponds to the angle for which the Radon transform reaches its maximum value (IV). It is worth highlighting that the processing described in [25] was slightly modified, we included interpolation and circular weighting to limit the effect of the default maxima at -45° and 45° of the Radon transform of a square homogeneous matrix.

The processing was repeated for all the depths of the phantom; then, the accuracy of the estimates was assessed in terms of root mean square error (RMSE) and absolute error (AE), by comparing the expected and the estimated fiber orientation.

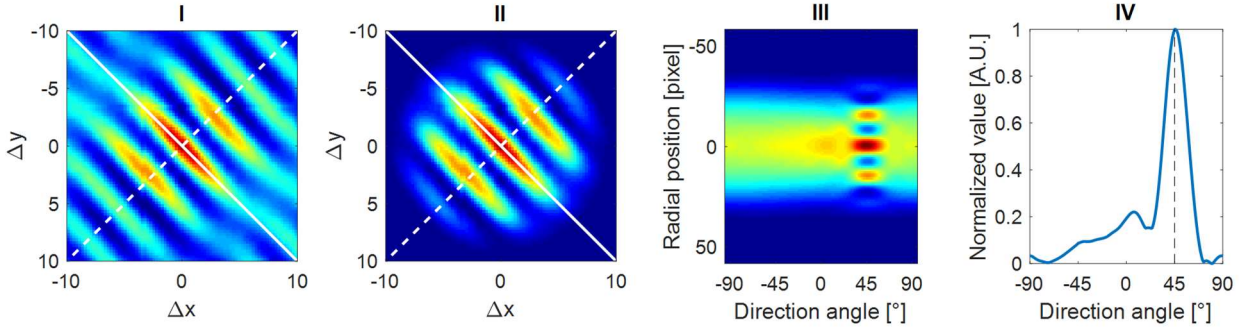

Fig. 1 Sketch of the processing steps implemented to estimate the fiber orientation. I) Interpolated spatial coherence map; II) Interpolated spatial coherence map after Tukey tapering; III) Radon transform of the tapered spatial coherence map; IV) Maximum of the Radon transform along the radial positions.

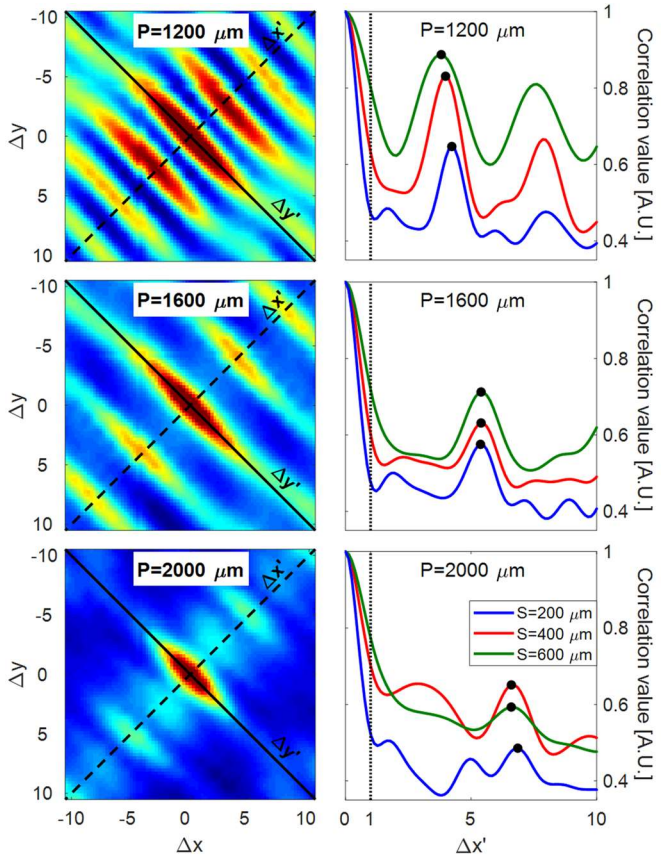

Fig. 2 Left panels: examples of SC maps obtained for S=600 μm and P=1200, 1600, 2000 μm from top to bottom, respectively. Right panels: SC profiles along Δx'-axis obtained for different S and P values; the dotted lines highlight the values of SC at Δx'=1; the black dots highlight the position of the peaks of the secondary lobes.

III. RESULTS

A. Spatial coherence

The left column in Fig. 2 shows examples of 2D spatial coherence maps obtained for fibers having S=600 μm and 3 different P values: 1200, 1600 and 2000 μm from top to bottom respectively. In these examples, the lags $(\Delta x, \Delta y)$ were limited to a maximum value of 10 elements. Qualitatively the maps clearly present: 1) a main lobe, whose origin is in (0,0) and its main direction is Δy'; 2) some secondary lobes parallel to the main one, whose distance along Δx', i.e. the direction orthogonal to Δy', is longer for higher P values. Similar results were obtained for different S values (200, 400, 600 μm) as shown on the right panels in Fig. 2. The latter highlight that the position of the secondary lobes peak only depends on the fiber pitch P, while the width of the main lobe shows a dependency on the fiber size S. As shown in Fig. 3, averaged over all models and all different fiber directions, the value of the SC at Δx'=1, i.e. an estimate of the main lobe width, linearly correlated with S (R^2=91.6%) while the main-to-secondary lobe lag distance linearly correlated with P (R^2=99.0%). In particular, the main-to-secondary lobe distance, on average, is equal to P; it corresponds to Δx' equal to P divided by the probe pitch (in this work set to 300 μm). The latter result is in agreement with the developed theory; indeed, considering the findings in (17), the autocorrelation of the scattering map in (18) should present secondary peaks at a distance P from the main lobe.

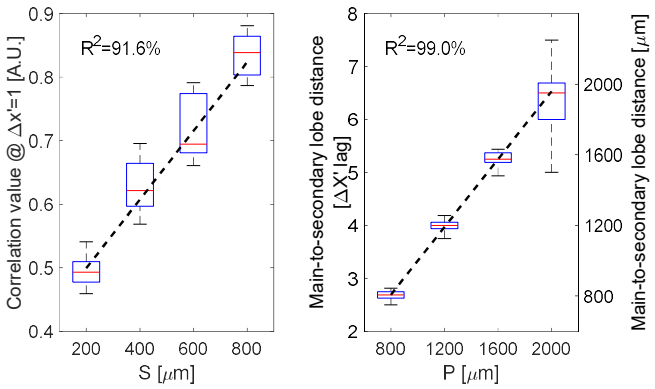

Fig. 3 Left: distribution of the correlation value computed at lag Δx'=1 for different fiber sizes S. Right: distribution of the main-to-secondary lobe distance for different fiber pitches P. The black dashed lines represent the linear fitting of the two distributions.

Hereinbefore, the illustrated results do not consider simulated model with P=400 μm since it is a special case. Indeed, it is worth remembering that the received echo signals, as well as the spatial coherence maps, are spatially sampled in the direction of the probe plane, with periodicity equal to the pitch among the elements of the probe. Hence, according to the Nyquist-Shannon sampling theorem, the direction of the fibers can only be detected when the periodicity of the fibers P is bigger than twice the pitch among the elements of the probe. An example of spatial coherence map obtained for S=200 μm and P=400 μm is shown in Fig. 4 highlighting that is indeed impossible to detect the direction of the main lobe due to aliasing.

B. Fiber orientation estimation

Fig. 5 shows examples of fiber orientation estimates obtained for fibers having S=600 μm and 3 different P values: 1200, 1600 and 2000 μm from left to right respectively, whose SC maps examples where also shown in Fig. 2. The estimated depth-trends (black traces) were compared to the expected ones showing good agreement. However, while the phantom was defined for the depth range [57; 63] mm, estimations were reliable only in the range [58; 62] mm. Outside that range the backscattered signals were mainly affected by the background, producing high intensity signals due to the reflections at the first and last interface of the phantom; this region corresponds to the black dashed lines in Fig. 5. For the tested modes, as shown in TABLE I, the RMSE was in the range [1.1°; 3.3°], while the absolute value of the average error was always lower than 1.1°. Worse results were in general obtained for S=800 μm fibers, while P does not seem to

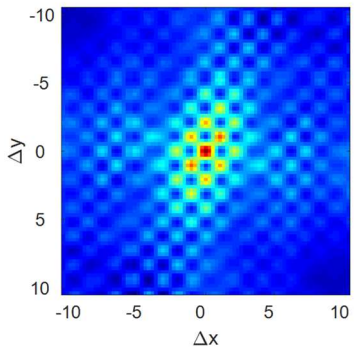

Fig. 4 Example of SC map obtained for S=200 μm and P=400 μm. The spatial undersampling generates aliasing, thus making impossible the detection of the direction of the fibers.

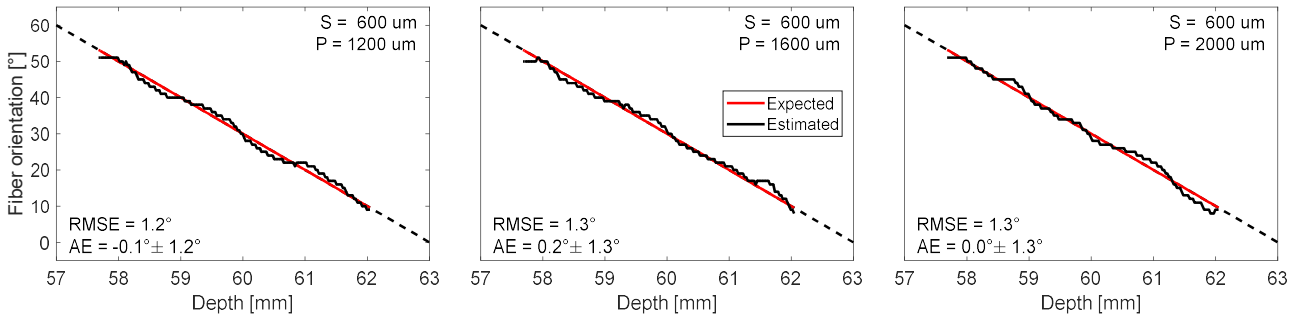

Fig. 5 Examples of fiber orientation estimation for the same models shown in Fig. 2 left panels, i.e. *S*=600 µm and *P*=1200, 1600, 2000 µm from left to right, respectively. The red lines are the reference expected values, the black lines are the estimated orientation values, while the gray dashed lines corresponds to the depth range where the echo signals were mainly affected by the reflections at the first and the last interfaces of the phantom.

TABLE I
RMSE AND ABSOLUTE ERROR OF THE FIBER ORIENTATION ESTIMATES

***S* [µm]**	**800**		**600**			**400**				**200**				
***P* [µm]**	**2000**	**1600**	**2000**	**1600**	**1200**	**2000**	**1600**	**1200**	**800**	**2000**	**1600**	**1200**	**800**	**400**
RMSE [°]	3.3	3.1	1.3	1.3	1.2	1.6	1.1	2.1	1.4	2.2	2.3	2.9	2.9	76.8
AE (mean±std) [°]	0.5± 3.2	1.1± 2.9	0.0± 1.3	0.2± 1.3	-0.1± 1.2	0.8± 1.4	-0.2± 1.1	-1.0± 1.9	0.5± 1.3	-0.8± 2.0	-0.6± 2.2	-0.7± 2.8	-0.5± 2.9	-67± 37.5

influence the accuracy of the estimates. The exception, as expected, is the special case with *P*=400 µm for which both RMSE and AE are higher than 67°, confirming that the spatial undersampling does not allow the estimation of the direction of the fibers.

IV. DISCUSSION AND CONCLUSION

In this paper we presented and validated, by computer simulation, a theoretical framework to have more insight on 3D ultrasound Backscatter Tensor Imaging. The theory showed that, for an unfocused transducer, the spatial coherence of the received echo field equals the autocorrelation of the spatial scattering amplitude distribution of the area illuminated by the transmitted beam. The theory was validated by simulating the echo signals received by a 32×32-element array transmitting a plane wave through a numeric phantom; the latter mimicking cardiac fibers as scatterers whose scattering amplitude was modulated according to a periodic function defining fiber size, pitch and orientation.

Examples of simulated SC maps of the received echo field were shown; they presented main and secondary lobes whose lateral width and distance have direct linear relationships with *S* and *P* respectively, as expected from the theory. Indeed, the SC maps should relate to the autocorrelation of the periodic scattering amplitude function, hence a wider *S* should correspond to a wider main beam and a bigger *P* should correspond to longer main-to-secondary beam distance as shown in Fig. 3. Moreover, through a Radon transform based algorithm [25], SC maps were exploited to estimate the cardiac fiber orientation at different depths of interest. The accuracy of the estimations was then assessed in terms of RMSE and AE, showing good agreement with the expected fiber orientation values (TABLE I).

In short, SC maps do not only carry information on fiber direction (i.e. the direction of highest correlation) but also have a one-to-one relationship with the fiber properties such as size and pitch; thus, SC can be exploited to determine the characteristics of the myocardium. However, we also showed that the minimum detectable *P* is equal to twice the pitch among the elements of the probe (2×300 µm in this work). Therefore, a lower limit applies to the minimum distance between fibers, that can be detected. Hence, concerning the initial doubt "What are we looking at?", it is unlikely that the proposed technique can detect the orientation of myocytes, indeed they are "*usually 120 µm long and 20-30 µm in diameter*" [3], but likely this approach allows detecting the direction of bigger structures such as bundles or sheets of several myocytes. It is worth highlighting that the same limitation may apply to the technique proposed in [25]; indeed it is based on the theories reported in [26], [27], but they rely on an approximation on the beamwidth of a focused transducer ([27] eq. B12), which is acceptable up to a maximum depth of 1.5 cm for the probe aperture used in [25].

APPENDIX A

Intermediate steps to demonstrate (14), mainly considering equations (10) and (13).

$$\mathcal{F}_{2D}\{R_{E_B}(x,y,0)\} = \mathcal{F}_{2D}\{E_B(x,y,0)\} \cdot \mathcal{F}_{2D}^{*}\{E_B(x,y,0)\} =$$

$$= [\mathcal{F}_{2D}\{E_R(x,y,z_F)\} \cdot \mathcal{F}_{2D}\{h_z(x,y,z_F)\}] \cdot$$
$$\cdot [\mathcal{F}_{2D}\{E_R(x,y,z_F)\} \cdot \mathcal{F}_{2D}\{h_z(x,y,z_F)\}]^{*} =$$

$$= [\mathcal{F}_{2D}\{E_R(x,y,z_F)\} \cdot \mathcal{F}_{2D}^{*}\{E_R(x,y,z_F)\}] \cdot$$
$$\cdot [\mathcal{F}_{2D}\{h_z(x,y,z_F)\} \cdot \mathcal{F}_{2D}^{*}\{h_z(x,y,z_F)\}] =$$

$$= \mathcal{F}_{2D}\{R_{E_R}(x,y,z_F)\} \cdot \mathcal{F}_{2D}\{R_{h_z}(x,y,z_F)\}$$

REFERENCES

[1] E. J. Benjamin *et al.*, "Heart Disease and Stroke Statistics—2018 Update: A Report From the American Heart Association," *Circulation*, p. CIR.0000000000000558, Jan. 2018.

[2] E. Wilkins *et al.*, "European Cardiovascular Disease Statistics 2017," *Eur. Heart Netw.*, Feb. 2017.

[3] S. Y. Ho, "Anatomy and myoarchitecture of the left ventricular wall in normal and in disease," *Eur. J. Echocardiogr. J. Work. Group Echocardiogr. Eur. Soc. Cardiol.*, vol. 10, no. 8, pp. iii3-7, Dec. 2009.

[4] R. H. Anderson, S. Y. Ho, K. Redmann, D. Sanchez-Quintana, and P. P. Lunkenheimer, "The anatomical arrangement of the myocardial cells making up the ventricular mass," *Eur. J. Cardiothorac. Surg.*, vol. 28, no. 4, pp. 517–525, Oct. 2005.

[5] M. J. Kocica, A. F. Corno, V. Lackovic, and V. I. Kanjuh, "The Helical Ventricular Myocardial Band of Torrent-Guasp," *Semin. Thorac. Cardiovasc. Surg. Pediatr. Card. Surg. Annu.*, vol. 10, no. 1, pp. 52–60, Jan. 2007.

[6] P. P. Sengupta *et al.*, "Left Ventricular Form and Function Revisited: Applied Translational Science to Cardiovascular Ultrasound Imaging," *J. Am. Soc. Echocardiogr.*, vol. 20, no. 5, pp. 539–551, May 2007.

[7] F. P. Mall, "On the muscular architecture of the ventricles of the human heart," *Am. J. Anat.*, vol. 11, no. 3, pp. 211–266, Mar. 1911.

[8] A. Keith, "Harveian Lecture on the functional anatomy of the heart," *Br. Med. J.*, vol. 1, no. 2987, pp. 361–363, Mar. 1918.

[9] T. Arts, K. D. Costa, J. W. Covell, and A. D. McCulloch, "Relating myocardial laminar architecture to shear strain and muscle fiber orientation," *Am. J. Physiol.-Heart Circ. Physiol.*, vol. 280, no. 5, pp. H2222–H2229, May 2001.

[10] A. G. Kléber and Y. Rudy, "Basic Mechanisms of Cardiac Impulse Propagation and Associated Arrhythmias," *Physiol. Rev.*, vol. 84, no. 2, pp. 431–488, Apr. 2004.

[11] D. A. Hooks, M. L. Trew, B. J. Caldwell, G. B. Sands, I. J. LeGrice, and B. H. Smaill, "Laminar Arrangement of Ventricular Myocytes Influences Electrical Behavior of the Heart," *Circ. Res.*, vol. 101, no. 10, pp. e103–e112, Nov. 2007.

[12] A. M. Varnava, P. M. Elliott, N. Mahon, M. J. Davies, and W. J. McKenna, "Relation between myocyte disarray and outcome in hypertrophic cardiomyopathy," *Am. J. Cardiol.*, vol. 88, no. 3, pp. 275–279, Aug. 2001.

[13] D. H. MacIver and A. L. Clark, "Contractile Dysfunction in Sarcomeric Hypertrophic Cardiomyopathy," *J. Card. Fail.*, vol. 22, no. 9, pp. 731–737, Sep. 2016.

[14] A. J. Marian and E. Braunwald, "Hypertrophic Cardiomyopathy: Genetics, Pathogenesis, Clinical Manifestations, Diagnosis, and Therapy," *Circ. Res.*, vol. 121, no. 7, pp. 749–770, Sep. 2017.

[15] P. F. Ferreira *et al.*, "In vivo cardiovascular magnetic resonance diffusion tensor imaging shows evidence of abnormal myocardial laminar orientations and mobility in hypertrophic cardiomyopathy," *J. Cardiovasc. Magn. Reson.*, vol. 16, p. 87, Nov. 2014.

[16] A. Nagler, C. Bertoglio, C. T. Stoeck, S. Kozerke, and W. A. Wall, "Maximum likelihood estimation of cardiac fiber bundle orientation from arbitrarily spaced diffusion weighted images," *Med. Image Anal.*, vol. 39, pp. 56–77, Jul. 2017.

[17] N. S. Jeffery, R. S. Stephenson, J. A. Gallagher, J. C. Jarvis, and P. G. Cox, "Micro-computed tomography with iodine staining resolves the arrangement of muscle fibres," *J. Biomech.*, vol. 44, no. 1, pp. 189–192, Jan. 2011.

[18] F. Varray, I. Mirea, M. Langer, F. Peyrin, L. Fanton, and I. E. Magnin, "Extraction of the 3D local orientation of myocytes in human cardiac tissue using X-ray phase-contrast micro-tomography and multi-scale analysis," *Med. Image Anal.*, vol. 38, pp. 117–132, May 2017.

[19] C. P. Fleming, C. M. Ripplinger, B. Webb, I. R. Efimov, and A. M. Rollins, "Quantification of cardiac fiber orientation using optical coherence tomography," *J. Biomed. Opt.*, vol. 13, no. 3, p. 030505, 2008.

[20] C. Fan and G. Yao, "Imaging myocardial fiber orientation using polarization sensitive optical coherence tomography," *Biomed. Opt. Express*, vol. 4, no. 3, pp. 460–465, Mar. 2013.

[21] P.-S. Jouk *et al.*, "Analysis of the fiber architecture of the heart by quantitative polarized light microscopy. Accuracy, limitations and contribution to the study of the fiber architecture of the ventricles during fetal and neonatal life," *Eur. J. Cardiothorac. Surg.*, vol. 31, no. 5, pp. 915–921, May 2007.

[22] H. Huang *et al.*, "Three-dimensional cardiac architecture determined by two-photon microtomy," *J. Biomed. Opt.*, vol. 14, no. 4, p. 044029, 2009.

[23] S. A. Wickline, E. D. Verdonk, and J. G. Miller, "Three-dimensional characterization of human ventricular myofiber architecture by ultrasonic backscatter.," *J. Clin. Invest.*, vol. 88, no. 2, pp. 438–446, Aug. 1991.

[24] W. N. Lee *et al.*, "Mapping Myocardial Fiber Orientation Using Echocardiography-Based Shear Wave Imaging," *IEEE Trans. Med. Imaging*, vol. 31, no. 3, pp. 554–562, Mar. 2012.

[25] C. Papadacci *et al.*, "Imaging the dynamics of cardiac fiber orientation in vivo using 3D Ultrasound Backscatter Tensor Imaging," *Sci. Rep.*, vol. 7, no. 1, p. 830, Apr. 2017.

[26] C. Papadacci, M. Tanter, M. Pernot, and M. Fink, "Ultrasound backscatter tensor imaging (BTI): analysis of the spatial coherence of ultrasonic speckle in anisotropic soft tissues," *IEEE Trans. Ultrason. Ferroelectr. Freq. Control*, vol. 61, no. 6, pp. 986–996, Jun. 2014.

[27] A. Derode and M. Fink, "Partial coherence of transient ultrasonic fields in anisotropic random media: Application to coherent echo detection," *J. Acoust. Soc. Am.*, vol. 101, no. 2, pp. 690–704, Feb. 1997.

[28] R. Mallart and M. Fink, "The van Cittert–Zernike theorem in pulse echo measurements," *J. Acoust. Soc. Am.*, vol. 90, no. 5, pp. 2718–2727, Nov. 1991.

[29] A. Derode and M. Fink, "Spatial coherence of ultrasonic speckle in composites," *IEEE Trans. Ultrason. Ferroelectr. Freq. Control*, vol. 40, no. 6, pp. 666–675, Nov. 1993.

[30] Durnin, "Exact solutions for nondiffracting beams. I. The scalar theory," *J. Opt. Soc. Am. A*, vol. 4, no. 4, p. 651, 1987.

[31] J.-Y. Lu, H. Zou, and J. F. Greenleaf, "Biomedical ultrasound beam forming," *Ultrasound Med. Biol.*, vol. 20, no. 5, pp. 403–428, Jan. 1994.

[32] J. Y. Lu and J. F. Greenleaf, "Nondiffracting X waves-exact solutions to free-space scalar wave equation and their finite aperture realizations," *IEEE Trans. Ultrason. Ferroelectr. Freq. Control*, vol. 39, no. 1, pp. 19–31, Jan. 1992.

[33] J. A. Jensen, "FIELD: A Program for Simulating Ultrasound Systems," *Med. Biol. Eng. Comput.*, vol. 34, no. Supplement 1, Part 1, pp. 351–353, 1996.

[34] A. Papoulis, *Systems and Transforms with Applications in Optics*. New York: McGraw-Hill Inc.,US, 1968.

[35] J. W. Goodman, *Introduction to Fourier Optics*. McGraw-Hill, 1968.

[36] T. L. Szabo, *Diagnostic Ultrasound Imaging: Inside Out*, 1st ed. Academic Press, 2004.

[37] J. A. Jensen and N. B. Svendsen, "Calculation of pressure fields from arbitrarily shaped, apodized, and excited ultrasound transducers," *IEEE Trans. Ultrason. Ferroelectr. Freq. Control*, vol. 39, no. 2, pp. 262–267, Mar. 1992.

[38] T. G. Feeman, *The Mathematics of Medical Imaging: A Beginner's Guide*. New York: Springer-Verlag, 2010.